



Bionic sunflower-like structure of polydopamine-confined NiFe-based quantum dots for electrocatalytic oxygen evolution reaction

Liguo Zhang^{a,b}, Wei Tang^{a,b}, Cheng Dong^c, Dongxue Zhou^{a,b}, Xueqing Xing^d, Wenjun Dong^{a,b,*}, Yihong Ding^e, Ge Wang^{a,**}, Mingyu Wu^f

^a Beijing Advanced Innovation Center for Materials Genome Engineering, Beijing Key Laboratory of Function Materials for Molecule & Structure Construction, School of Materials Science and Engineering, University of Science and Technology Beijing, Beijing 100083, PR China

^b Shunde Graduate School of University of Science and Technology Beijing, Foshan 528399, PR China

^c School of Materials Science and Engineering, Shandong University of Technology, Zibo 255049, PR China

^d Beijing Synchrotron Radiation Facility, Institute of High Energy Physics, Chinese Academy of Sciences, Beijing 100049, PR China

^e Institute of Theoretical Chemistry, Jilin University, Changchun 130023, PR China

^f Institute of Nuclear Materials, School of Materials Science and Engineering, University of Science and Technology Beijing, Beijing 100083, PR China

ARTICLE INFO

Keywords:

Bionic sunflower structure
Space-confined effect
Quantum dots
In-situ reconstruction
Oxygen evolution reaction

ABSTRACT

NiFe-based nanostructures have been attracting attentions as a promising non-noble metal electrocatalysts for oxygen evolution reaction in alkaline. In this paper, a bionic sunflower-like NiFe-polydopamine film was prepared via self-polymerization of dopamine-Ni²⁺/Fe³⁺ followed by partial pyrolysis process. In the films, NiO quantum dots are embedded in Fe-coupled polydopamine due to the space-confined effect of PDA. The self-activation process effect led to in-situ reconstruction of the generation of NiOOH and the migration of Fe sites to NiOOH surface. Abundant Fe sites on the NiOOH surface facilitated formation of stable O* intermediate. Moreover, the coordination-confined effect of PDA for Fe ions in the PDA network gave the PDANF catalyst excellent durability. The NiFe-polydopamine film exhibited excellent intrinsic OER activity with a low overpotential of 254.1 mV for 10 mA cm⁻² and an unprecedentedly low Tafel slope of 23.3 mV dec⁻¹.

1. Introduction

Electrocatalytic water splitting into hydrogen and oxygen is one of the effective strategies to converse and store renewable energy sources [1–3]. However, the oxygen evolution reaction (OER, 4OH⁻ → 2H₂+O₂+ 4e⁻ in base) with a four-electron transfer is limited by the efficiency of the electrochemical systems for the sluggish kinetics process [4,5]. Therefore, highly active electrocatalysts for reducing the overpotential of OER are required to improve the efficiency of water splitting [2,6]. Up to now, IrO₂ and RuO₂ are the benchmarks for electrocatalytic OER reaction with considerable turnover frequencies at moderate overpotentials [7–9]. However, the extremely high cost and the scarcity of these elements greatly restrict their large-scale industrial application [10,11]. Therefore, non-precious metal substitutes with high catalytic activity and stability are urgently required [12–14]. Great efforts have been made to explore earth-abundant first-row (3d) transition

metal-based catalysts (such as Fe, Ni, Co, and Mn) that exhibit suitable adsorption free energy for oxygen evolution intermediates in volcano-type plots [15–17]. Moreover, the electronic structure can be adjusted via precise regulating elementary composition to increase OER catalytic activity [18–21].

Fe-doped Ni-based materials have been considered as the promising OER catalysts due to the high activity and stability in alkaline environment [22–24]. Electron transfer between the adjacent Ni and Fe atoms is crucial for regulating the electronic structure around the active site and enhancing OER activity [25–27]. Furthermore, the improved OER activity of NiFe-based electrocatalysts is closely related to the Fe sites. Fe in (Ni, Fe)OOH identified as highly active sites by the in situ X-ray absorption spectroscopy [28,29]. The presence of Fe(IV) in NiFe hydroxide/oxyhydroxide was demonstrated by the operando Mössbauer spectroscopy and in situ X-ray absorption near-edge structure [30,31]. The high spin d⁴ Fe(IV) sites on the surface of Fe-doped β-NiOOH

* Corresponding author at: Beijing Advanced Innovation Center for Materials Genome Engineering, Beijing Key Laboratory of Function Materials for Molecule & Structure Construction, School of Materials Science and Engineering, University of Science and Technology Beijing, Beijing 100083, PR China.

** Corresponding author.

E-mail addresses: wdong@ustb.edu.cn (W. Dong), gewang@mater.ustb.edu.cn (G. Wang).

<https://doi.org/10.1016/j.apcatb.2021.120833>

Received 30 August 2021; Received in revised form 1 October 2021; Accepted 15 October 2021

Available online 23 October 2021

0926-3373/© 2021 Elsevier B.V. All rights reserved.

catalysts facilitate the formation of O^* ($Fe=O$) species [32,33], which is crucial for O-O bond formation and OER execution. Significantly, the outstanding OER activity of NiFe-based catalysts depends on the Fe sites at the edge or defects, rather than Fe in bulk phase [34–36]. Moreover, the surface iron sites suffer severe dissolution during the OER process, resulting in reduced catalyst activity [18,29,37]. Therefore, creating rich and sustainable Fe sites on the surface of Ni-based materials are an important strategy for further improving OER activity and stability.

In this paper, NiFe-polydopamine film (PDANF) was prepared by a polymerizing dopamine (DOPA) coordinated with Ni^{2+} and Fe^{3+} , followed by calcining at low temperature. Due to the smaller binding energy of Ni to polydopamine (PDA) than that of Fe to PDA (demonstrated by density flooding theory (DFT) calculations), NiO quantum dots (QDs) were formed and embedded in the Fe^{3+} -coupled PDA film like the sunflower seeds mosaicked in sunflower plates. During cyclic voltammetry activation, the Fe^{3+} ligated to PDA migrate to the surface of NiOOH QDs in-situ converted from NiO DQs. The in-situ reconstruction during activation is responsible for the dramatic increase in OER performance of PDANF film. In detail, NiOOH QDs as a stable substrate to anchor Fe sites stably. Moreover, the charge accumulation on NiOOH accelerated the charge exchange between Ni and Fe sites through the co-linked lattice oxygen, which promoted the formation of stable Fe^{+4} -O intermediates to improve OER reaction kinetics. In addition, the strong Fe^{3+} -coordination ability of the PDA network resulted in the coordination-limiting effect of PDA where the PDA network released and recaptured of Fe^{3+} to avoid reduction in catalytic activity due to the loss of Fe ions in PDANF film. The PDANF catalyst shows a low overpotential of 254.1 mV for 10 mA cm^{-2} and an unprecedentedly low Tafel slope of 23.3 mV dec^{-1} . Due to enrichment of Fe sites on the surface of NiOOH QDs, the mass activity of PDANF is more than 32.3 times that of NiFe LDH and 200.8 times that of the benchmark commercial RuO_2 . Finally, the strategy of in situ reconstruction for metal-organic catalyst developed here provide new ideas for the development of inexpensive electrocatalysts with high performance and stability.

2. Experimental section

2.1. Chemicals

Dopamine hydrochloride (DOPA-HCl, $\geq 98.0\%$, Aladdin), Cobalt(II) nitrate hexahydrate ($Co(NO_3)_2 \cdot 6H_2O$, $\geq 98.0\%$, Aladdin), Nickel(II) nitrate hexahydrate ($Ni(NO_3)_2 \cdot 6H_2O$, $\geq 98.0\%$, Energy Chemical), Iron(III) nitrate nonahydrate ($Fe(NO_3)_3 \cdot 9H_2O$, $\geq 99.99\%$, Energy Chemical), Tris(hydroxymethyl)methyl aminomethane (Tris, $\geq 99.8\%$, Aladdin), Hydrochloric acid (36–38%, Sinopharm), Nafion (5 wt% in alcohol and water, Sigma-Aldrich), ruthenium oxide (RuO_2 , Sigma-Aldrich), Carbon cloths (CC, HCP330N). All reagents were used as received without further purification.

2.2. Materials preparation

Synthesis of PDANF catalyst. A piece of CC ($2 \times 2 \text{ cm}^2$) was soaked in acetone and sonicated for 30 min to remove surface oil and rinsed with deionized water. 0.02 mmol (3.8 mg) of DA-HCl, 0.004 mmol (1.6 mg) of $Fe(NO_3)_3 \cdot 9H_2O$ were homogeneously dissolved into 2 mL deionized water in a 50 mL glass beaker. 0.016 mmol (4.6 mg) of $Ni(NO_3)_2 \cdot 6H_2O$ were dissolved into 10 mL Tris-buffer solution and added to the above solution to form metal-DOPA complex. And then, a piece of CC ($3 \times 3 \text{ cm}^2$) was immersed in the above solution followed by shaking for 12 h. The precursor was washed several times with deionized water and ethanol, and dried at 70 °C for 12 h. To obtain stable catalyst, the as-synthesized PDANF precursor was then annealed at 300 °C under N_2 gas flow for 0.5 h with a ramp rate of 5 °C min^{-1} .

Synthesis of PDA-metal catalyst. The same methods were used for the others PDA-metal samples, except different metal salts (for PDANi, 0.02 mmol of $Ni(NO_3)_2 \cdot 6H_2O$; for PDAFe, 0.02 mmol of $Fe(NO_3)_3 \cdot 9H_2O$; for

PDANCF, 0.008 mmol of $Ni(NO_3)_2 \cdot 6H_2O$, 0.008 mmol of $Co(NO_3)_2 \cdot 6H_2O$ and 0.004 mmol of $Fe(NO_3)_3 \cdot 9H_2O$; for PDANC, 0.01 mmol of $Ni(NO_3)_2 \cdot 6H_2O$ and 0.01 mmol of $Co(NO_3)_2 \cdot 6H_2O$; for PDACF, 0.016 mmol of $Co(NO_3)_2 \cdot 6H_2O$ and 0.004 mmol of $Fe(NO_3)_3 \cdot 9H_2O$; for PDANi₈Fe₁, 0.0178 mmol of $Ni(NO_3)_2 \cdot 6H_2O$ and 0.0022 of $Fe(NO_3)_3 \cdot 9H_2O$; for PDANi₃Fe₂, 0.012 mmol of $Ni(NO_3)_2 \cdot 6H_2O$ and 0.008 of $Fe(NO_3)_3 \cdot 9H_2O$; for PDANi₂Fe₃, 0.08 mmol of $Ni(NO_3)_2 \cdot 6H_2O$ and 0.012 of $Fe(NO_3)_3 \cdot 9H_2O$).

Synthesis of NiFe LDH/CC. The NiFe LDH/CC was synthesized by hydrothermal method. A piece of CC ($2 \times 2 \text{ cm}^2$) was soaked in acetone and sonicated for 30 min to remove surface oil, then rinsed with ethanol and dried at 80 °C for 4 h. 1 mmol (0.291 g) of $Ni(NO_3)_2 \cdot 6H_2O$, 0.25 mmol (0.101 g) of $Fe(NO_3)_3 \cdot 9H_2O$, 0.4 g of urea 0.08 g of NH_4F were added to 21 mL of deionized water and stirred for 30 min to form a homogeneous solution in a Teflon vessel (25 mL). The carbon cloth is immersed in the reaction solution. The Teflon vessel was transferred to a stainless-steel autoclave and then heated at 120 °C for 6 h. After cooling to room temperature, NiFe LDH/CC was washed three times with water and ethanol and dried at 80 °C.

2.3. Characterizations

The morphological information of PDANF was examined with Field-emission scanning electron microscopy (FESEM; Hitachi, SU8010), and the high resolution transmission electron microscopy (HRTEM; Tecnai G2 F20 S-TWIN(200KV)). The corresponding element mapping images were captured with image corrector. The Raman spectra were performed on a Renishaw inVia reflex Raman microscope under an excitation of 532 nm laser light with the power of 20 mW. The X-ray photoelectron spectroscopy (XPS) was recorded on Thermo Scientific Escalab 250Xi. All the peaks are calibrated with C 1s spectrum at binding energy of 284.8 eV. The XAFS experiments were performed at beamline 4B9A of Beijing Synchrotron Radiation Facility (BSRF). All the acquired XAFS data were processed by the IFEFFIT software packages.

2.4. Electrochemical measurements

The CHI 660D electrochemical workstation with a three-electrode system was used to test the electrochemical properties of the materials at room temperature. The graphite rod was used as the counter electrode, the calibrated Hg/HgO electrode as the reference electrode. The PDA-metal electrodes were cropped to $0.3 \times 1 \text{ cm}^2$, and used as the working electrode directly. In the OER test, 20 cycles of cyclic voltammetry (CV) were first recorded at 10 mV s^{-1} from 0.415 to 0.615 V (vs Hg/HgO) for the activation and in-situ transformation in 1 M KOH solution (pH = 14). The linear sweep voltammetry polarization curves were measured at 5 mV s^{-1} and 90% iR corrected, and all the measured potentials were referred to reversible hydrogen electrode (RHE) via the Nernst equation ($E_{RHE} = E_{Hg/HgO} + 0.0592 \times pH + E_{Hg/HgO}^0$). The Tafel plots were constructed by the Tafel equation, $\eta = b \log j + a$, where “j” is the current density, “b” is the Tafel slope, and “a” is the intercept relative to the exchange current density. The stability of the catalysts was measured by chronoamperometry at OER overpotential of 300 mV. Electrochemical impedance spectroscopy (EIS) was carried out from 106 Hz to 0.01 Hz to evaluate the charge transfer ability of the catalysts [38]. The electrochemical active surface area (ECSA) of the catalysts was assessed by cyclic voltammetry (CV) in a non-faradaic potential region (1.23–1.33 V vs. RHE) at different scan rates to achieve double layer capacitance (Cdl) value of the catalysts. The current density difference between anodic current density (j_a) and cathodic current density (j_c) at a given potential value was calculated. A plotted line based on $\Delta j = (j_a - j_c)/2$ and the scan rate was built, and then fitted by a linear regression curve. The Cdl value calculated from the slope of the fitting curve is consistent with the reactive surface area of the materials. The OER Faradic efficiency of PDANF was tested by gas collection method.

3. Results and discussion

3.1. Structural analysis and DFT calculation

The two-step preparation of PDANF electrode is schematically depicted in Fig. 1a. The dopamine monomers were ligated with Fe and Ni, and self-polymerized on the surface of carbon cloth to form a film. The precursors were treated at 300 °C to form the PDANF film with a sunflower structure. The binding energies of Ni^{2+} and Fe^{3+} with DOPA were calculated by DFT calculation [39,40]. All models were geometrically optimized using the Gaussian software package at the density functional theory (DFT) level by means of unrestricted B3LYP [41,42] functional. For more details on the calculations, please refer to the Supporting Materials. In the ground state, the binding energy of Fe^{3+} with ligand DOPA monomer (− 21.93 eV) is stronger than that of Ni^{2+} (− 17.94 eV), which indicates the coordination of Fe^{3+} with PDA is more stable than that of Ni^{2+} with PDA (Table S1 and S2). Ni^{2+} were aggregated in the pore of the PDA to form NiO QDs during the heat treatment owing to the relatively weak binding energy of Ni^{2+} with the PDA. In addition, the coordination-confined effect of PDA stabilized the Fe^{3+} to atomically dispersed in PDANF film.

The morphology and structure of the PDANF catalyst before and after activation were characterized by electron microscope analysis. The initial PDANF film is approximately 20 nm in thickness and attached on CC tightly (Fig. 2c and S1a). In the initial sample, NiO QDs are uniformly dispersed on the PDANF film in an ultra-small structure (particle size of 2–4 nm) owing to the space-confined effect of PDA (Fig. 2a and S1b). The high-resolution TEM image (HRTEM) showed that an interplanar spacing of 0.21 nm corresponds to the (200) planes of NiO (Fig. 2b). The high-angle annular dark-field scanning TEM (HAADF STEM) and the electron energy loss spectroscopy (EELS) elemental mapping clearly demonstrate the uniform distribution of Ni, Fe, and O elements on CC (Fig. 2f). After CV activation, the structure of the PDANF film was well maintained (Fig. 2d), and NiO QDs were in situ oxidized to NiOOH QDs. The in-situ transformation of NiO to NiOOH agreed well with the previously reported results [43]. The lattice fringe with the distance of 0.24 nm can be assigned to (002) facet of β -NiOOH (Fig. 2e). Notably, the ultra-small structure of the NiOOH QDs in the activated PDANF was inherited owing to the spatial domain-limiting effect of PDA. Moreover, such ultra-small NiOOH QDs exposed more highly active edge sites in favor of improving OER performance.

3.2. Local structure and valence analysis

The electron states and local structures of Ni and Fe in PDANF before

and after activation were further investigated by synchrotron-based X-ray absorption near edge structure (XANES) spectra [44]. The corresponding first-order derivative spectra were plotted in order to compare clearly the K-edge jump positions of Ni and Fe in PDANF before and after activation. Firstly, due to the presence of NiO QDs in pristine PDANF sample, XANES at Ni K-edge shows close spectroscopic feature to that of standard NiO sample. After electrochemical activation, XANES at Ni K-edge shows a significant change of electronic property of Ni sites (Fig. 3a). The similar pre-edge profiles of Ni in pristine PDANF, activated PDANF and NiO imply a six-coordination structure of Ni (inset in Fig. 3a). The higher position of 1s to 4p jump energy for Ni in the activated PDANF compared to that in initial sample confirms the formation of Ni^{3+} during the electrochemical process (Fig. 3b) [45]. For the XANES at Fe K-edge, the dramatic difference in the spectral characteristics of pristine PDANF films with Fe_2O_3 excludes the presence of Fe_2O_3 (Fig. 3c). Importantly, the intensity of pre-edge peak of Fe in PDANF decreases markedly after activation (inset in Fig. 3c), which is attributed to the better symmetry of coordination environment of the Fe after activation. Moreover, the presence of Fe^{4+} is similarly demonstrated by the high energy shift of the Fe 1s to 4p absorption threshold for activation PDANF sample (Fig. 3d) [46–49].

In addition, the coordination environments of Fe and Ni were further studied from the extended X-ray absorption fine structure (EXAFS). No phase correction was carried out for Fourier-transformed (FT) k^2 -weighted R spatial data (Fig. 3e and S6). For the initial sample, the Ni-O coordination number of 6.2 and the Ni-O distance of 2.04 Å are consistent with the hexa-coordination structure and Ni-O bond length in NiO lattice (Table S3). After electrochemical activation, the appearance of Ni-M (M = Ni or Fe) coordination peak at 2.73 Å suggests the lower disorder of NiOOH QDs than that of NiO QDs (Fig. 3e and S6a). In FT EXAFS spectra of Fe, the intensity of Fe-O coordination peak in pristine PDANF film much lower than that in Fe_2O_3 , implying that the coordination number of Fe in the initial PDANF is much less than that in Fe_2O_3 (Fig. S6b). After electrochemical activation, a Fe-M coordination peak appears at 2.76 for the activated PDANF film (Fig. 3e and S6b). The lower Fe-O and Fe-M coordination numbers of Fe compared to Ni-O and Ni-M in the activated PDANF mean that Fe migrates to the surface of NiOOH QDs and forms unsaturated Fe sites. In addition, the shorter bond length of Fe is due to the relaxation effect of Fe on the NiOOH surface (Table S4).

X-ray photoelectron spectroscopy (XPS) was performed to verify the changes in electronic structure and valence states for Ni and Fe in PDANF before and after the OER activation. As shown in Fig. 4a, High-resolution Ni 2p spectrum of the pristine PDANF shows two sets of doublets peaks at 855.5 and 873.5 eV corresponding to the $\text{Ni} 2p_{3/2}$ and

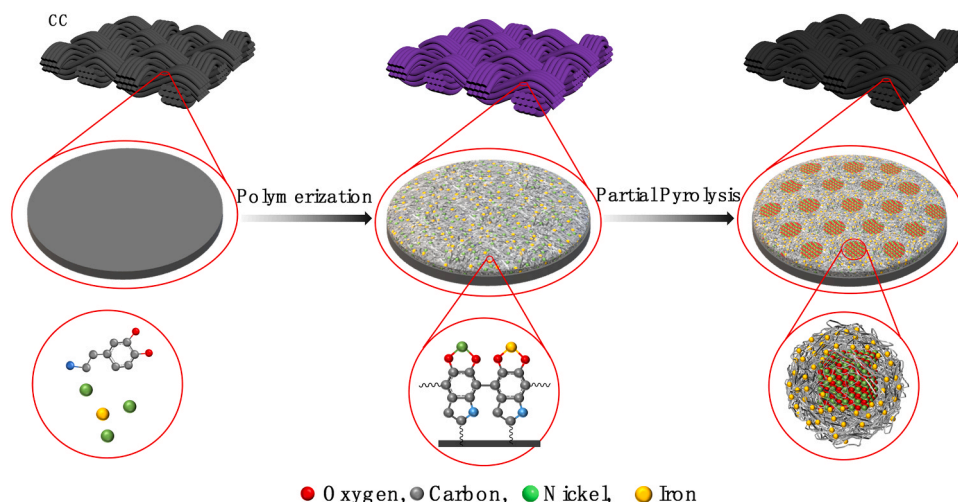


Fig. 1. Schematic diagram for the fabrication of PDANF electrode.

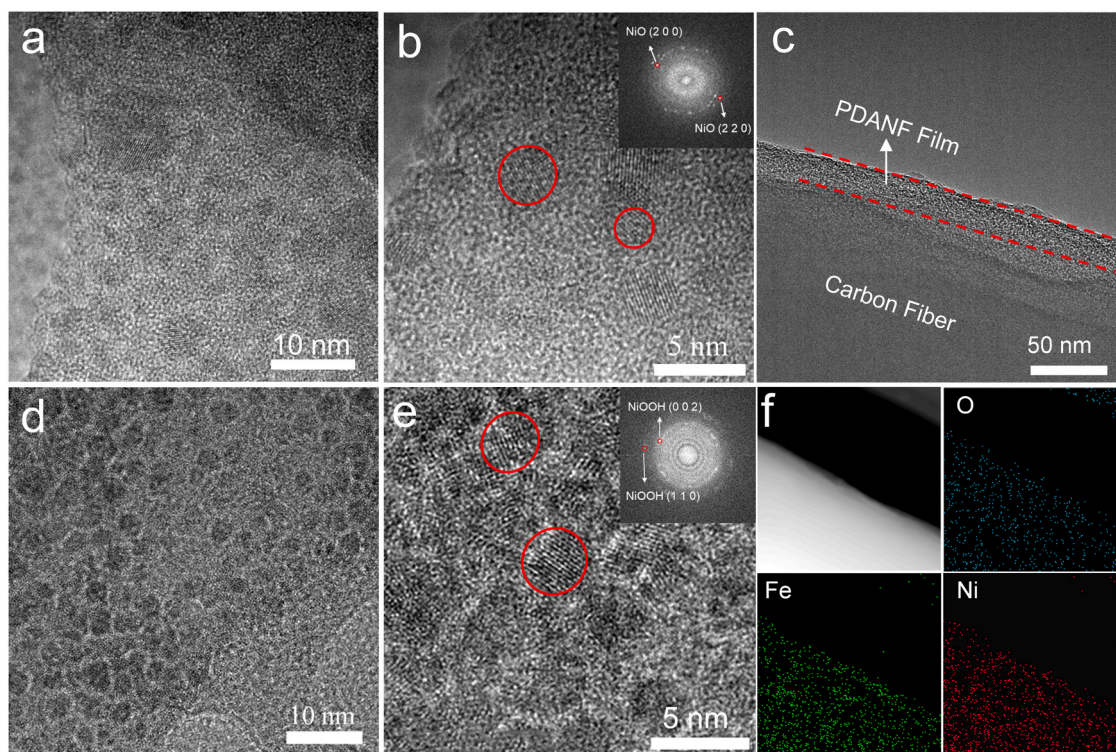


Fig. 2. Election microscope analysis of the PDANF sample. (a), (b) and (c) HRTEM images of sample before the activation; (d) and (e) HRTEM images of activated sample; (f) the HAADF result and EELS mapping images of O, Ni and Fe on the PDANF.

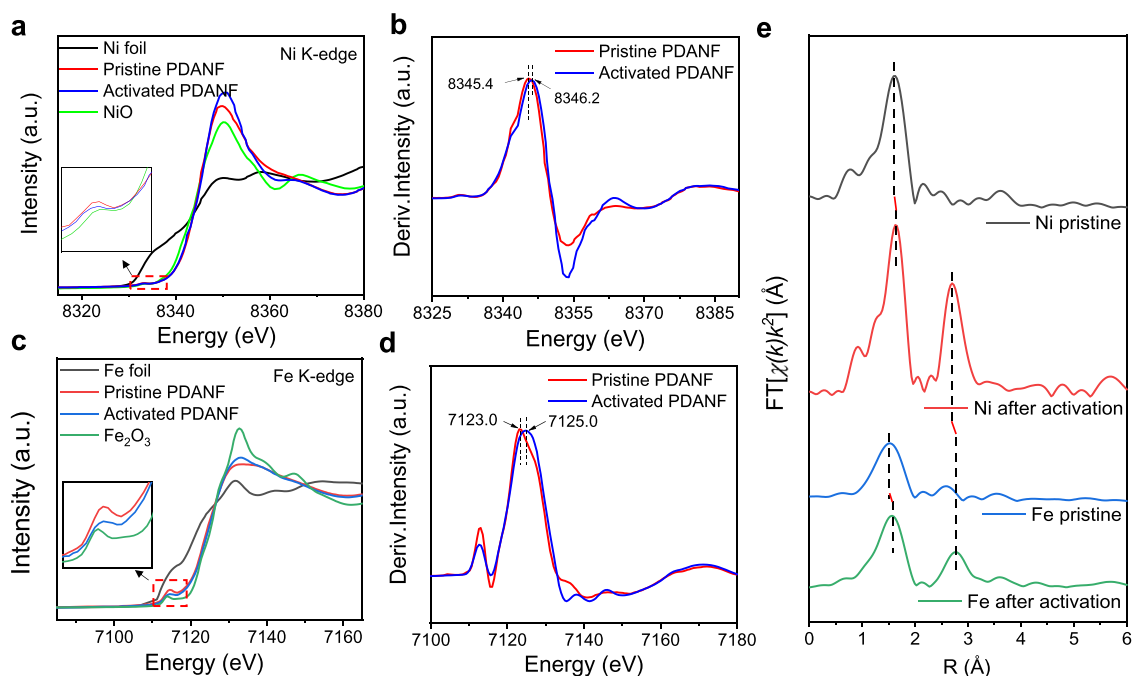


Fig. 3. (a) and (b) Ni K-edge XANES spectra, Fe K-edge XANES spectra, and the enlarge the pre-edge curve inseted the corresponding image; (c) and (d) first-order derivative spectra of Ni and Fe K-edge XANES spectra in PDANF; (e) FT curves of Ni, Fe K-edge EXAFS $k^2\chi(k)$ functions obtained from the XANES spectra of PDANF before and after activation, respectively.

$2p_{1/2}$ of Ni^{2+} , respectively [38,50]. Meanwhile, the peaks at 861.5 eV and 879.7 eV were assigned to the accompanying satellite peak of Ni $2p_{3/2}$ and Ni $2p_{1/2}$ [51]. During the activation process, NiO DQs were in situ oxidized to NiOOH QDs by potential-induced phase transformation with two new peaks at binding energy of 857.2 eV and 875.0 eV, which are

ascribed to Ni^{3+} $2p_{3/2}$ and $2p_{1/2}$ (Fig. 4a) [52,53]. In the high-resolution Fe 2p spectrum of the pristine PDANF sample (Fig. 4b), two broad peaks at the binding energy of 712.0 and 725.0 eV can be ascribed to Fe^{3+} coordinated by PDA, which is consistent with the XPS results of PDAFe (Fig. S4). In addition, a pair of small peaks at 711.2 and 724.4 eV are

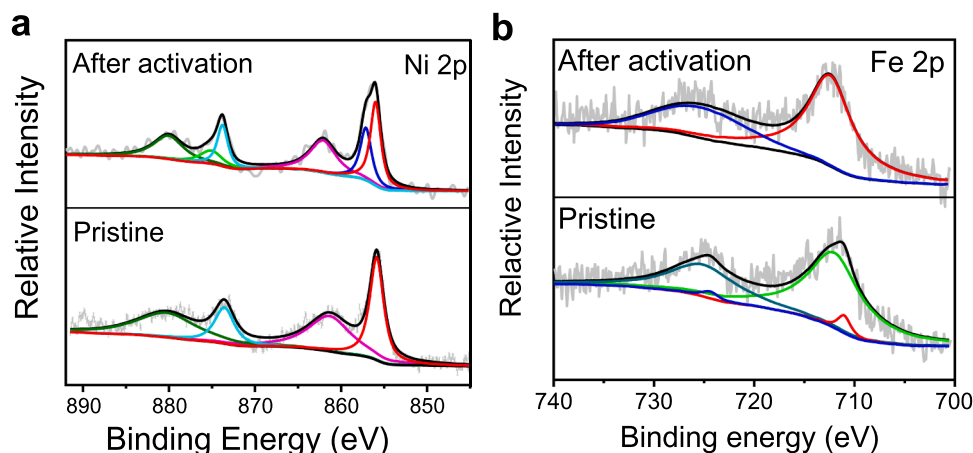


Fig. 4. X-ray photoelectron spectroscopy (XPS) narrow-scan spectra of PDANF before and after OER activation process. (a) Ni 2p and (b) Fe 2p.

attributed to slight Fe^{3+} incorporated into NiO lattice [54]. Notably, the presence of Fe_2O_3 is excluded due to the absence of vibrational satellite peaks at 719 and 732 eV [54,55]. Upon activation, the electron binding

energies of Fe $2p_{3/2}$ and $2p_{1/2}$ were transferred to the high energy positions of 712.4 and 725.3 eV due to the oxidation of Fe. The XPS results demonstrated the in-situ reconstruction driven by electrochemistry for

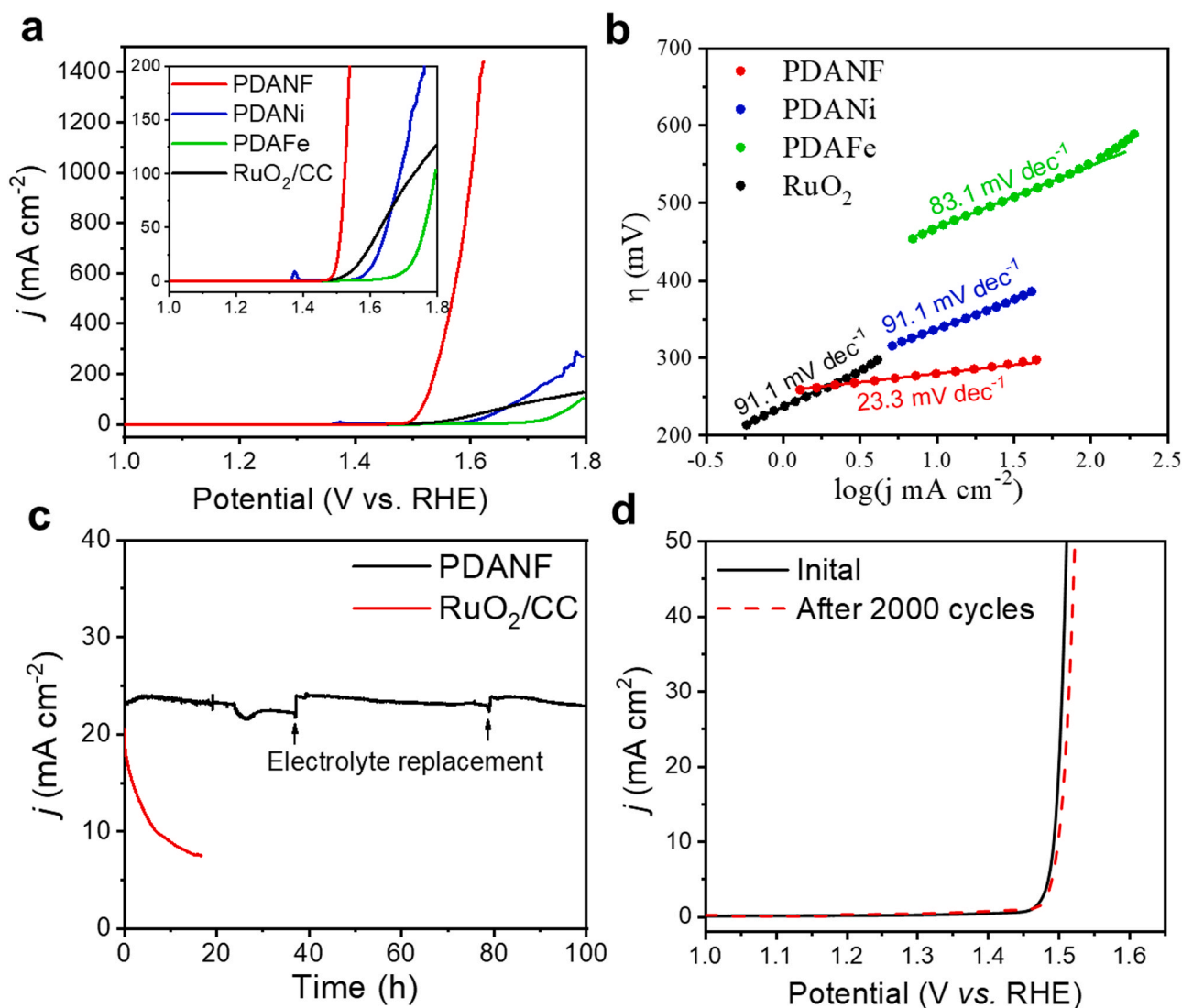


Fig. 5. Electrocatalytic OER performance in 1 M KOH aqueous solution. (a). 90% iR-corrected linear sweep voltammetry (LSV) polarization curves of PDANF, PDANi, PDAFe, and RuO₂/CC samples at a scan rate of 5 mV s⁻¹. (b). Corresponding Tafel plots of the LSV curves in (a). (c). Stability test of the PDANF and RuO₂/CC at 1.53 V vs. RHE. (d). LSV curves of initial PDANF and the same electrode after 2000 CV cycles.

PDANF film consistent with the XANS and EXAFS results.

3.3. Electrocatalytic performance

The OER capability of the PDANF electrode was studied using a typical three-electrode system in 1.0 M KOH aqueous solution. The activation CV curve of PDANF sample is partially shown in Fig. S8a. The oxidation and reduction peaks below OER potential were attributed to the oxidation charge accumulation and release of the NiOOH QDs. The accumulation of oxidation charges with increasing numbers of cv cycles suggests that more NiOOH QDs are activated, accompanied by enhanced dynamic activity of the PDANF films. Moreover, decrease onset potential indicates an enhancement in intrinsic catalytic activity. To explore the relationship between the kinetic activity of the PDANF catalyst and the oxidation charge accumulation, the Tafel slope of CV polarization curves were plotted against the corresponding amount of reduced charge (equal to the oxidation charge). Obviously, the square of the inverse of the Tafel slope shows a good linear relationship with the corresponding oxidation charge over a range (Fig. S8b). The results suggested that the charge accumulation on Fe-doped NiOOH QDs accelerated the charge exchange between Ni and Fe sites through the co-linked lattice oxygen, and promoted the formation of Fe^{+4} and Ni^{4+} . A synergistic effect between Fe^{4+} (stabilizing the M-O radical state) and Ni^{4+} (promoting O—O bond formation) promotes the kinetics of the OER reaction [56–58]. However, considering the effects of catalyst loading limitation, mass transfer and charge transport, ineffective charge accumulation occurs when the catalyst loading reaches a certain amount. In contrast, PDANi and PDAFe films showed insignificant change in electrochemical activity during CV activation.

The electrocatalytic OER performance of the PDANF, PDANi, PDAFe, and RuO_2/CC were measured under the same condition. The linear sweep voltammetry (LSV) was recorded in the range of 0.901.80 V (vs. RHE) at 5 mV s^{-1} scan rate. PDANF sample exhibits the superior performance in electrochemical OER activity, which reveals a much lower overpotential of 254.1 mV, 282 mV and 293 mV at 10 mA cm^{-2} , 50 mA cm^{-2} and 100 mA cm^{-2} , respectively (Fig. 5a). In contrast, the reference samples of PDANi, PDAFe and RuO_2/CC required 347 mV, 474 mV and 310 mV at 10 mA cm^{-2} , respectively. Tafel slopes for these catalysts are calculated to study the kinetics of water oxidation (Fig. 5b). The calculated Tafel slopes for PDANF, PDANi, PDAFe and RuO_2/CC were 23.3, 91.1, 83.1 and 91.1 mV dec^{-1} respectively, demonstrating rapid reaction kinetics of PDANF film [59]. In addition, PDA-bimetallic catalysts with different Ni and Fe contents were tested and all demonstrated higher OER performance than the monometallic catalysts (Fig. S9a). These results fully demonstrate the synergistic effect of Ni and Fe on the enhancement of electrocatalytic OER activity. To study the electron transport capacity of the catalyst, the EIS was measured in an aqueous 1 M KOH solution at potential of 1.5 V (vs. RHE) (Fig. S9b). The EIS data of these film electrodes were fitted with the equivalent circuit (inset in Fig. S9b). R_s , C_d and R_{ct} correspond to the solution resistance, the double-layer capacitance and the charge-transfer resistance respectively. The fitted EIS data are exhibited in Table S5. The charge transfer resistance of PDANF is much lower than that other PDA-NiFe electrodes, which indicating the excellent OER reaction kinetics of PDANF. Obviously, the rapid charge exchange between Ni and Fe through lattice oxygen enhances the electron transport kinetics of PDANF.

The high durability of electrocatalyst is also a crucial evaluation parameter for energy conversion systems [60,61]. The chronoamperometry tests of the PDANF electrodes and RuO_2/CC were performed under potential of 1.53 V (RHE) (Fig. 5c). The PDANF electrode exhibited a stable OER current density (about 23 mA cm^{-2}) for 100 h. During the test, the electrolyte solution was changed at the 36th and 79th hour, and the current densities were returned to the initial state. In comparison, the current density of the RuO_2/CC catalyst dramatically decreased to half of original value (18 mA cm^{-2}) within 8 h. After being subjected to 2000 CV cycles, the overpotential of PDANF only increased

by 3 mV at 10 mA cm^{-2} compared to the initial activated sample (Fig. 5d). The structure, and composition for PDANF samples were characterized before and after 100 h durability test (Fig. S13). The membrane structure was maintained. Interestingly, porous structures were generated on PDANF film, due to impact of O_2 gas generated at the Fe-NiOOH QDs. Furthermore, the energy-dispersive X-ray spectroscopy (EDS) elemental mapping images demonstrate that the nickel, iron, and oxygen elements are uniformly distributed on the surface of carbon fiber before and after activation. The results illustrate the excellent stability of performance, structural, and compositional for PDANF catalyst. Ultra-high electrocatalytic stability of PDANF catalyst was attributed to two factors. Firstly, the strong coordination of the reticulated PDA can recapture the Fe^{3+} to avoid reduction in catalytic activity due to the loss of Fe^{3+} , which avoided the reduction of activity due to the depletion of Fe sites on the NiOOH surface during the OER process. Secondly, the space-confined effect of PDA results in excellent structural stability of Fe-doped NiOOH QDs.

To further investigate the water oxidation performance of the PDANF catalyst, OER activation of NiFe LDH/CC, which is widely considered to be one of the best catalysts for OER, was chosen for comparison. As shown as LSV polarization curve (Fig. 6a), the PDANF electrode shows higher geometric current density of 147.6 mA cm^{-2} at 300 mV overpotential compared with NiFe LDH/CC of 47.7 mA cm^{-2} . The Tafel slope of 23.3 mV dec^{-1} for PDANF catalyst was much lower than the 49.8 mV dec^{-1} for NiFe LDH/CC (Fig. 6b). Furthermore, the mass activity of PDANF of 1314.8 A g^{-1} is more than 32.3 times larger than that (40.6 A g^{-1}) of NiFe LDH/CC at the overpotential of 300 mV (Fig. 6c). The current density was normalized by electrochemical surface area (ECSA) (Fig. 6c). Similarly, the PDANF electrode exhibited 15.1 times the electrocatalytic OER activity of NiFe LDH/CC at 300 mV overpotential. The in-situ reconstitution of PDANF catalyst leads to a synergistic catalytic effect between abundant Fe sites and NiOOH QDs, which enhances catalytic activity for OER.

4. Conclusions

In summary, bionic sunflower-like structure of Fe-coordinated PDA encapsulating NiO QDs was successful prepared by a simple polymerization method followed by calcination at low temperature. In situ reconstruction of PDANF film in electrochemical activation was investigated to explain the remarkably increase in electrocatalytic OER performance. In the electrochemical process, NiOOH QD is in-situ transformed from NiO QD, storing enough oxidation charges for the four-electron OER process. While the abundant Fe species migrate off the PDA to the NiOOH QDs surface and promote the formation of Fe-O intermediates. Due to the enrichment of Fe sites on the surface of NiOOH QDs, PDANF film exhibits much higher OER performance than NiFe LDH/CC and RuO_2/CC . Moreover, the coordination-confined effect of PDA network for Fe ions achieves excellent stability of the composition and properties for PDANF film. Thus, the proposed strategy of structural design and in-situ reconstitution provide new insight for studying metal-organic electrocatalysts.

CRedit authorship contribution statement

Wenjun Dong: Designed the experiments, designed the article structure, and revised manuscript revisions. **Liguo Zhang:** Designed the experiments, designed the article structure, and revised manuscript revisions, synthesized the materials, carried out most of the structural characterization, and authored the manuscript, performed characterization and analysis and cowrote the paper, performed the synchrotron XAS test. **Wei Tang:** Designed the experiments, synthesized the materials, carried out most of the structural characterization, and authored the manuscript. **Cheng Dong:** Performed characterization and analysis and cowrote the paper. **Dongxue Zhou:** Performed characterization and analysis and cowrote the paper. **Xueqing Xing:** Performed the

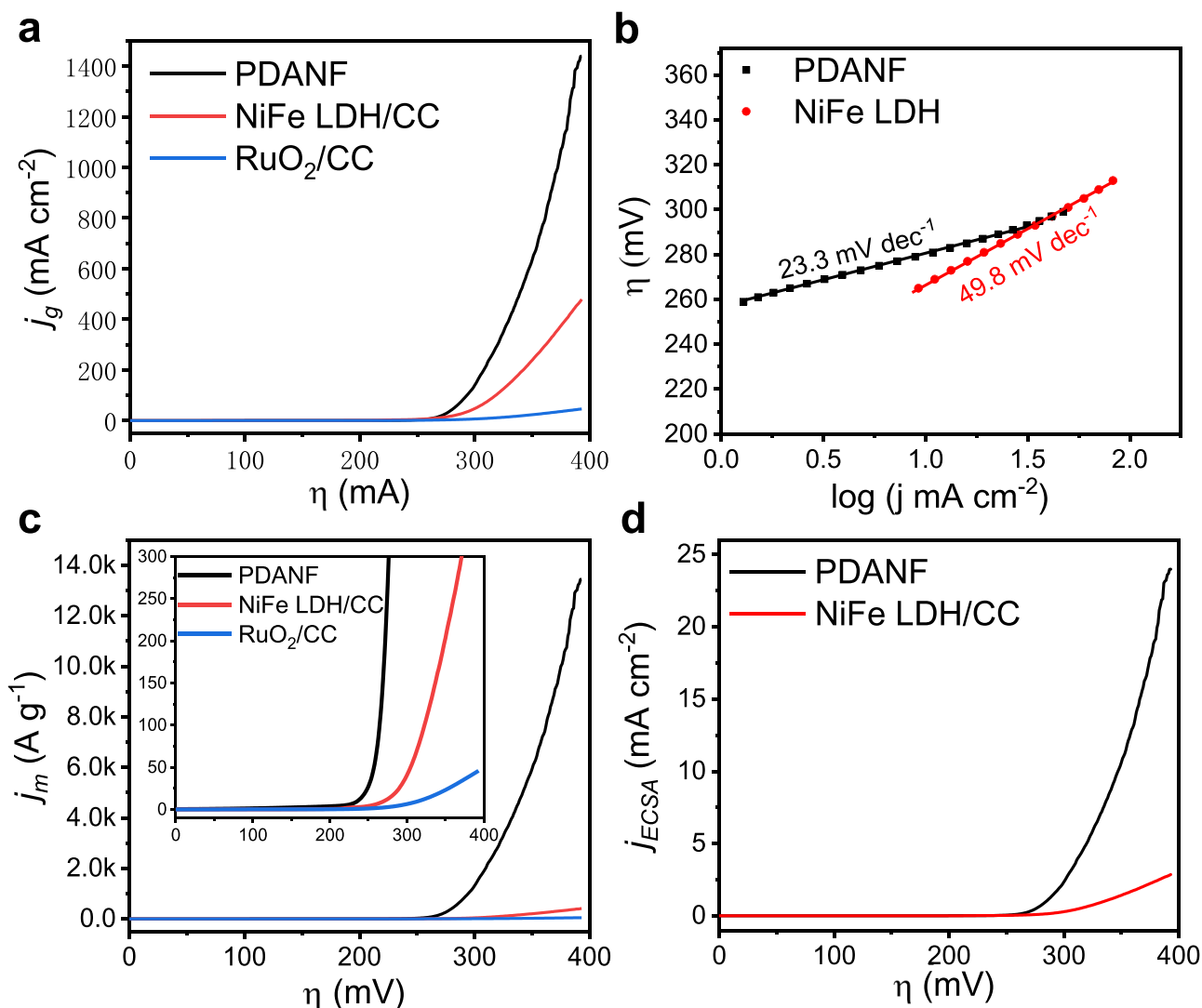


Fig. 6. (a) 90% iR-corrected linear sweep voltammetry (LSV) polarization curves of reference PDANF, NiFe LDH, and RuO₂ loaded on CC samples at a scan rate of 5 mV s⁻¹. (b) Corresponding Tafel plots. (c) Mass activity of the PDANF catalyst, NiFe LDH, and RuO₂. The inset is the magnification of red frame. (d) ECSA normalized LSV curve for PDANF film and NiFe LDH/CC electrodes.

synchrotron XAS test. **Yihong Ding:** Performed the DFT calculations. **Mingyu Wu:** Performed the DFT calculations. **Ge Wang:** Revised the paper. All authors contributed to the interpretation of the results and improvement of the paper.

Declaration of Competing Interest

The authors declare that they have no known competing financial interests or personal relationships that could have appeared to influence the work reported in this paper.

Acknowledgments

This work was supported by the National Natural Science Foundation of China (52071027 and 51872025), Capital's Funds for Health Improvement and Research (2021-1G-4291), the Beijing Municipal Natural Science Foundation (2212038), the National Defense Basic Scientific Research (JCKY2019110C036), Scientific and Technological Innovation Foundation of Foshan (BK21BE008), Foshan Innovation Research Funding for University Teacher (2020XCC06), the Fundamental Research Funds for the Central Universities (FRF-GF-20-03A and FRF-GF-19-006B), and the National Key R&D Program of China

(2017YFA0403100) for financial support. The computing work is supported by USTB MatCom of Beijing Advanced Innovation Center for Materials Genome Engineering.

Appendix A. Supporting information

Supplementary data associated with this article can be found in the online version at [doi:10.1016/j.apcatb.2021.120833](https://doi.org/10.1016/j.apcatb.2021.120833).

References

- [1] Z.W. Seh, J. Kibsgaard, C.F. Dickens, I.B. Chorkendorff, J.K. Nørskov, T. F. Jaramillo, Combining theory and experiment in electrocatalysis: insights into materials design, *Science* 355 (2017), <https://doi.org/10.1126/science.aad4998>.
- [2] J. Song, C. Wei, Z.-F. Huang, C. Liu, L. Zeng, X. Wang, Z.J. Xu, A review on fundamentals for designing oxygen evolution electrocatalysts, *Chem. Soc. Rev.* 49 (2020) 2196–2214, <https://doi.org/10.1039/c9cs00607a>.
- [3] H. Yan, Y. Xie, A. Wu, Z. Cai, L. Wang, C. Tian, X. Zhang, H. Fu, Anion-modulated HER and OER activities of 3D Ni-V-based interstitial compound heterojunctions for high-efficiency and stable overall water splitting, *Adv. Mater.* 31 (2019), 1901174, <https://doi.org/10.1002/adma.201901174>.
- [4] Y. Chen, S. Ji, C. Chen, Q. Peng, D. Wang, Y. Li, Single-atom catalysts: synthetic strategies and electrochemical applications, *Joule* 2 (2018) 1242–1264, <https://doi.org/10.1016/j.joule.2018.06.019>.

- [5] L. Li, P. Wang, Q. Shao, X. Huang, Recent progress in advanced electrocatalyst design for acidic oxygen evolution reaction, *Adv. Mater.* (2021), 2004243, <https://doi.org/10.1002/adma.202004243>.
- [6] J. Mohammed-Ibrahim, A review on NiFe-based electrocatalysts for efficient alkaline oxygen evolution reaction, *J. Power Sources* 448 (2020), 227375, <https://doi.org/10.1016/j.jpowsour.2019.227375>.
- [7] C. Wang, L. Jin, H. Shang, H. Xu, Y. Shiraishi, Y. Du, Advances in engineering RuO₂ electrocatalysts towards oxygen evolution reaction, *Chin. Chem. Lett.* 32 (2021) 2108–2116, <https://doi.org/10.1016/j.ccl.2020.11.051>.
- [8] L.-W. Chen, H.-W. Liang, Ir-based bifunctional electrocatalysts for overall water splitting, *Catal. Sci. Technol.* 11 (2021) 4673–4689, <https://doi.org/10.1039/d1cy00650a>.
- [9] S.H. Ye, Z.X. Shi, J.X. Feng, Y.X. Tong, G.R. Li, Activating CoOOH porous nanosheet arrays by partial iron substitution for efficient oxygen evolution reaction, *Angew. Chem. Int. Ed.* 57 (2018) 2672–2676, <https://doi.org/10.1002/anie.201712549>.
- [10] X. Wang, H. Xiao, A. Li, Z. Li, S. Liu, Q. Zhang, Y. Gong, L. Zheng, Y. Zhu, C. Chen, D. Wang, Q. Peng, L. Gu, X. Han, J. Li, Y. Li, Constructing NiCo/Fe₃O₄ heterostructures within MOF-74 for efficient oxygen evolution reactions, *J. Am. Chem. Soc.* 140 (2018) 15336–15341, <https://doi.org/10.1021/jacs.8b08744>.
- [11] X. Yue, X.P. Qin, Y.D. Chen, Y. Peng, C.H. Liang, M. Feng, X.Z. Qiu, M.H. Shao, S. M. Huang, Constructing active sites from atomic-scale geometrical engineering in spinel oxide solid solutions for efficient and robust oxygen evolution reaction electrocatalysts, *Adv. Sci.* 8 (2021), 2101653, <https://doi.org/10.1002/adv.202101653>.
- [12] X. Feng, Q. Jiao, W. Chen, Y. Dang, Z. Dai, S.L. Suib, J. Zhang, Y. Zhao, H. Li, C. Feng, Cactus-like NiCo₂S₄@NiFe LDH hollow spheres as an effective oxygen bifunctional electrocatalyst in alkaline solution, *Appl. Catal. B Environ.* 286 (2021), 119869, <https://doi.org/10.1016/j.apcatb.2020.119869>.
- [13] Z.-P. Wu, X.F. Lu, S.-Q. Zang, X.W. Lou, Non-noble-metal-based electrocatalysts toward the oxygen evolution reaction, *Adv. Funct. Mater.* 30 (2020) 800, <https://doi.org/10.1002/adfm.201910274>.
- [14] H. Xu, Z.-X. Shi, Y.-X. Tong, G.-R. Li, Porous microrod arrays constructed by carbon-confined NiCo@NiCoO₂ Core@Shell nanoparticles as efficient electrocatalysts for oxygen evolution, *Adv. Mater.* 30 (2018), 1705442, <https://doi.org/10.1002/adma.201705442> (e1705442-e1705442).
- [15] C. Chen, Y. Tuo, Q. Lu, H. Lu, S. Zhang, Y. Zhou, J. Zhang, Z. Liu, Z. Kang, X. Feng, D. Chen, Hierarchical trimetallic Co-Ni-Fe oxides derived from core-shell structured metal-organic frameworks for highly efficient oxygen evolution reaction, *Appl. Catal. B Environ.* 287 (2021), 119953, <https://doi.org/10.1016/j.apcatb.2021.119953>.
- [16] J. Ding, T. Fan, K. Shen, Y. Li, Electrochemical synthesis of amorphous metal hydroxide microarrays with rich defects from MOFs for efficient electrocatalytic water oxidation, *Appl. Catal. B Environ.* 292 (2021), 120174, <https://doi.org/10.1016/j.apcatb.2021.120174>.
- [17] G. Hai, X. Jia, K. Zhang, X. Liu, Z. Wu, G. Wang, High-performance oxygen evolution catalyst using two-dimensional ultrathin metal-organic frameworks nanosheets, *Nano Energy* 44 (2018) 345–352, <https://doi.org/10.1016/j.nanoen.2017.11.071>.
- [18] D.Y. Chung, P.P. Lopes, P.F.B.D. Martins, H. He, T. Kawaguchi, P. Zapol, H. You, D. Tripkovic, D. Strmcnik, Y. Zhu, S. Seifert, V.R. Stamenkovic, N. M. Markovic, Dynamic stability of active sites in hydr(oxy)oxides for the oxygen evolution reaction, *Nat. Energy* 5 (2020) 222–230, <https://doi.org/10.1038/s41560-020-0576-y>.
- [19] M.-I. James, M. Harb, Tuning the electronic structure of the earth-abundant electrocatalysts for oxygen evolution reaction (OER) to achieve efficient alkaline water splitting - a review, *J. Energy Chem.* 56 (2021) 299–342, <https://doi.org/10.1016/j.jechem.2020.08.001>.
- [20] X. Zhao, X.Q. Li, Y. Yan, Y.L. Xing, S.C. Lu, L.Y. Zhao, S.M. Zhou, Z.M. Peng, J. Zeng, Electrical and structural engineering of cobalt selenide nanosheets by Mn modulation for efficient oxygen evolution, *Appl. Catal. B Environ.* 236 (2018) 569–575, <https://doi.org/10.1016/j.apcatb.2018.05.054>.
- [21] J.W. Zhao, C.F. Li, Z.X. Shi, J.L. Guan, G.R. Li, Boosting lattice oxygen oxidation of perovskite to efficiently catalyze oxygen evolution reaction by FeOOH decoration, *Research* 2020 (2020), 6961578, <https://doi.org/10.34133/2020/6961578>.
- [22] Z.W. Gao, J.Y. Liu, X.M. Chen, X.L. Zheng, J. Mao, H. Liu, T. Ma, L. Li, W.C. Wang, X.W. Du, Engineering NiO/NiFe LDH intersection to bypass scaling relationship for oxygen evolution reaction via dynamic tridimensional adsorption of intermediates, *Adv. Mater.* 31 (2019), 1804769, <https://doi.org/10.1002/adma.201804769>.
- [23] J. Zhang, J. Liu, L. Xi, Y. Yu, N. Chen, S. Sun, W. Wang, K.M. Lange, B. Zhang, Single-atom Au/NiFe layered double hydroxide electrocatalyst: probing the origin of activity for oxygen evolution reaction, *J. Am. Chem. Soc.* 140 (2018) 3876–3879, <https://doi.org/10.1021/jacs.8b00752>.
- [24] X. Guo, X. Zheng, X. Hu, Q. Zhao, L. Li, P. Yu, C. Jing, Y. Zhang, G. Huang, B. Jiang, C. Xu, F. Pan, Electrostatic adsorbing graphene quantum dot into nickel-based layered double hydroxides: electron absorption/donor effects enhanced oxygen electrocatalytic activity, *Nano Energy* 84 (2021), 105932, <https://doi.org/10.1016/j.nanoen.2021.105932>.
- [25] J. Wang, L. Ji, Z. Chen, In situ rapid formation of a nickel-iron-based electrocatalyst for water oxidation, *ACS Catal.* 6 (2016) 6987–6992, <https://doi.org/10.1021/acscatal.6b01837>.
- [26] J. Zhao, J.J. Zhang, Z.Y. Li, X.H. Bu, Recent progress on NiFe-based electrocatalysts for the oxygen evolution reaction, *Small* 16 (2020), e2003916, <https://doi.org/10.1002/smll.202003916>.
- [27] C.F. Li, J.W. Zhao, L.J. Xie, J.Q. Wu, Q. Ren, Y. Wang, G.R. Li, Surface-adsorbed carboxylate ligands on layered double hydroxides/metal-organic frameworks promote the electrocatalytic oxygen evolution reaction, *Angew. Chem. Int. Ed.* 60 (2021) 18129–18137, <https://doi.org/10.1002/anie.202104148>.
- [28] D. Friebe, M.W. Louie, M. Bajdich, K.E. Sanwald, Y. Cai, A.M. Wise, M.-J. Cheng, D. Sokaras, T.-C. Weng, R. Alonso-Mori, R.C. Davis, J.R. Bargar, J.K. Nørskov, A. Nilsson, A.T. Bell, Identification of highly active Fe sites in (Ni,Fe)OOH for electrocatalytic water splitting, *J. Am. Chem. Soc.* 137 (2015) 1305–1313, <https://doi.org/10.1021/ja511559d>.
- [29] S. Anantharaj, S. Kundu, S. Noda, “The Fe Effect”: a review unveiling the critical roles of Fe in enhancing OER activity of Ni and Co based catalysts, *Nano Energy* 80 (2021), 105514, <https://doi.org/10.1016/j.nanoen.2020.105514>.
- [30] J.Y.C. Chen, L. Dang, H. Liang, W. Bi, J.B. Gerken, S. Jin, E.E. Alp, S.S. Stahl, Operando analysis of NiFe and Fe oxyhydroxide electrocatalysts for water oxidation: detection of Fe⁴⁺ by Mossbauer spectroscopy, *J. Am. Chem. Soc.* 137 (2015) 15090–15093, <https://doi.org/10.1021/jacs.5b10699>.
- [31] D. Wang, J. Zhou, Y. Hu, J. Yang, N. Han, Y. Li, T.K. Sham, In situ X-ray absorption near-edge structure study of advanced NiFe(OH)_x electrocatalyst on carbon paper for water oxidation, *J. Phys. Chem. C* 119 (2015) 19573–19583, <https://doi.org/10.1021/acs.jpcc.5b02685>.
- [32] J.M.P. Martinez, E.A. Carter, Unraveling oxygen evolution on iron-doped beta-nickel oxyhydroxide: the key role of highly active molecular-like sites, *J. Am. Chem. Soc.* 141 (2019) 693–705, <https://doi.org/10.1021/jacs.8b12386>.
- [33] Y. Hao, Y. Li, J. Wu, L. Meng, J. Wang, C. Jia, T. Liu, X. Yang, Z.-P. Liu, M. Gong, Recognition of surface oxygen intermediates on NiFe oxyhydroxide oxygen-evolving catalysts by homogeneous oxidation reactivity, *J. Am. Chem. Soc.* 143 (2021) 1493–1502, <https://doi.org/10.1021/jacs.0c11307>.
- [34] M.B. Stevens, C.D.M. Trang, L.J. Enman, J. Deng, S.W. Boettcher, Reactive Fe-sites in Ni/Fe (oxy)hydroxide are responsible for exceptional oxygen electrocatalysis activity, *J. Am. Chem. Soc.* 139 (2017) 11361–11364, <https://doi.org/10.1021/jacs.7b07117>.
- [35] C. Peng, N. Ran, G. Wan, W. Zhao, Z. Kuang, Z. Lu, C. Sun, J. Liu, L. Wang, H. Chen, Engineering active Fe sites on nickel-iron layered double hydroxide through component segregation for oxygen evolution reaction, *ChemSuschem* 13 (2020) 811–818, <https://doi.org/10.1002/cssc.201902841>.
- [36] T. Wu, S. Sun, J. Song, S. Xi, Y. Du, B. Chen, W.A. Sasangka, H. Liao, C.L. Gan, G. G. Scherer, L. Zeng, H. Wang, H. Li, A. Grimaud, Z.J. Xu, Iron-facilitated dynamic active-site generation on spinel CoAl₂O₄ with self-termination of surface reconstruction for water oxidation, *Nat. Catal.* 2 (2019) 763–772, <https://doi.org/10.1038/s41429-019-0325-4>.
- [37] R. Farhat, J. Dhainy, L.I. Halaoui, OER catalysis at activated and codeposited NiFe-Oxo/Hydroxide thin films is due to postdeposition surface-Fe and is Not sustainable without Fe in solution, *ACS Catal.* 10 (2020) 20–35, <https://doi.org/10.1021/acscatal.9b02580>.
- [38] X. Guo, X. Hu, D. Wu, C. Jing, W. Liu, Z. Ren, Q. Zhao, X. Jiang, C. Xu, Y. Zhang, N. Hu, Tuning the bifunctional oxygen electrocatalytic properties of core-shell Co₃O₄@NiFe LDH catalysts for Zn-Air batteries: effects of interfacial cation valences, *ACS Appl. Mater. Interfaces* 11 (2019) 21506–21514, <https://doi.org/10.1021/acsami.9b04217>.
- [39] J. Heimann, L. Morrow, R.E. Anderson, A.R. Barron, Understanding the relative binding ability of hydroxyfullerene to divalent and trivalent metals, *Dalton Trans.* 44 (2015) 4380–4388, <https://doi.org/10.1039/c4dt03376k>.
- [40] Q. Liu, X. Lu, L. Li, H. Zhang, G. Liu, H. Zhong, H. Zeng, Probing the reversible Fe³⁺-DOPA-mediated bridging interaction in mussel foot protein¹, *J. Phys. Chem. C* 120 (2016) 21670–21677, <https://doi.org/10.1021/acs.jpcc.6b07482>.
- [41] Lee, Yang, Development of the colle-salvetti correlation-energy formula into a functional of the electron density, *Phys. Rev. B Condens. Matter* 37 (1988) 785–789, <https://doi.org/10.1103/PhysRevB.37.785>.
- [42] P.J.D. Stephens, F.J. Chabalowski, C.F. Frisch, M.J. Ab, Initio calculation of vibrational absorption and circular dichroism spectra using density functional force fields, *J. Chem. Phys.* 98 (1994) 11623–11627, <https://doi.org/10.1021/j100096a001>.
- [43] X. Hu, G. Luo, X. Guo, Q. Zhao, R. Wang, G. Huang, B. Jiang, C. Xu, F. Pan, Origin of the electrocatalytic oxygen evolution activity of nickel phosphides: in-situ electrochemical oxidation and Cr doping to achieve high performance, *Sci. Bull.* 66 (2021) 708–719, <https://doi.org/10.1016/j.scib.2020.11.009>.
- [44] X. Hu, G. Luo, Q. Zhao, D. Wu, T. Yang, J. Wen, R. Wang, C. Xu, N. Hu, Ru single atoms on N-doped carbon by spatial confinement and ionic substitution strategies for high-performance Li-O₂ batteries, *J. Am. Chem. Soc.* 142 (2020) 16776–16786, <https://doi.org/10.1021/jacs.0c07317>.
- [45] S.-Y. Lee, I.-S. Kim, H.-S. Cho, C.-H. Kim, Y.-K. Lee, Resolving potential-dependent degradation of electrodeposited Ni(OH)₂ catalysts in alkaline oxygen evolution reaction (OER): in situ XANES studies, *Appl. Catal. B Environ.* 284 (2021), 119729, <https://doi.org/10.1016/j.apcatb.2020.119729>.
- [46] J.L. Martinez, S.A. Lutz, H. Yang, J. Xie, J. Telser, B.M. Hoffman, V. Carta, M. Pink, Y. Losovyj, J.M. Smith, Structural and spectroscopic characterization of an Fe(VI) bis(imido) complex, *Science* 370 (2020) 356–359, <https://doi.org/10.1126/science.abd3054>.
- [47] G.L. Fu, W.W. Li, J.Y. Zhang, M.S. Li, C.J. Li, N. Li, Q. He, S.B. Xi, D.C. Qi, J. L. MacManus-Driscoll, J. Cheng, K.H. Zhang, Facilitating the deprotonation of OH to O through Fe⁴⁺-induced states in perovskite LaNiO₃ enables a fast oxygen evolution reaction, *Small* 17 (2021), 2006930, <https://doi.org/10.1002/smll.202006930>.
- [48] N. Li, R.G. Hadt, D. Hayes, L.X. Chen, D.G. Nocera, Detection of high-valent iron species in alloyed oxidic cobaltates for catalysing the oxygen evolution reaction, *Nat. Commun.* 12 (2021) 4218, <https://doi.org/10.1038/s41467-021-24453-6> (4218–4218).

- [49] S. Das, S. Bhattar, L. Liu, Z. Wang, S. Xi, J.J. Spivey, S. Kawi, Effect of partial Fe substitution in $\text{La}_{0.9}\text{Sr}_{0.1}\text{NiO}_3$ Perovskite-derived catalysts on the reaction mechanism of methane dry reforming, *ACS Catal.* 10 (2020) 12466–12486, <https://doi.org/10.1021/acscatal.0c01229>.
- [50] S. Nangan, Y.C. Ding, A.Z. Alhakemy, Y.J. Liu, Z.H. Wen, Hybrid alkali-acid urea-nitrate fuel cell for degrading nitrogen-rich wastewater, *Appl. Catal. B Environ.* 286 (2021), 119892, <https://doi.org/10.1016/j.apcatb.2021.119892>.
- [51] H. Van Chinh, D. Khang Ngoc, V.G. Gomes, Hybrid Ni/NiO composite with N-doped activated carbon from waste cauliflower leaves: a sustainable bifunctional electrocatalyst for efficient water splitting, *Carbon* 157 (2020) 515–524, <https://doi.org/10.1016/j.carbon.2019.09.080>.
- [52] Z. Wu, Z. Zou, J. Huang, F. Gao, NiFe_2O_4 nanoparticles/NiFe layered double-hydroxide nanosheet heterostructure array for efficient overall water splitting at large current densities, *ACS Appl. Mater. Interfaces* 10 (2018) 26283–26292, <https://doi.org/10.1021/acsami.8b07835>.
- [53] B. Kim, A. Oh, M.K. Kabiraz, Y. Hong, J. Joo, H. Baik, S.-I. Choi, K. Lee, NiOOH exfoliation-free nickel octahedra as highly active and durable electrocatalysts toward the oxygen evolution reaction in an alkaline electrolyte, *ACS Appl. Mater. Interfaces* 10 (2018) 10115–10122, <https://doi.org/10.1021/acsami.7b19457>.
- [54] K. Fominykh, P. Chernev, I. Zaharieva, J. Sicklinger, G. Stefanic, M. Doeblinger, A. Mueller, A. Pokharel, S. Boecklein, C. Scheu, T. Bein, D. Fattakhova-Rohlfing, Iron-doped nickel oxide nanocrystals as highly efficient electrocatalysts for alkaline water splitting, *ACS Nano* 9 (2015) 5180–5188, <https://doi.org/10.1021/acsnano.5b00520>.
- [55] T. Yamashita, P. Hayes, Analysis of XPS spectra of Fe^{2+} and Fe^{3+} ions in oxide materials, *Appl. Surf. Sci.* 254 (2008) 2441–2449, <https://doi.org/10.1016/j.apsusc.2007.09.063>.
- [56] H.N. Nong, L.J. Falling, A. Bergmann, M. Klingenhof, H.P. Tran, C. Spori, R. Mom, J. Timoshenko, G. Zichittella, A. Knop-Gericke, S. Piccinin, J. Perez-Ramirez, B. R. Cuenya, R. Schlögl, P. Strasser, D. Teschner, T.E. Jones, Key role of chemistry versus bias in electrocatalytic oxygen evolution, *Nature* 587 (2020) 408–413, <https://doi.org/10.1038/s41586-020-2908-2>.
- [57] P. Zhang, W. Wang, H. Wang, Y. Li, C. Cui, Tuning hole accumulation of metal oxides promotes the oxygen evolution rate, *ACS Catal.* 10 (2020) 10427–10435, <https://doi.org/10.1021/acscatal.0c02882>.
- [58] K. Wang, H.F. Du, S. He, L. Liu, K. Yang, J.M. Sun, Y.H. Liu, Z.Z. Du, L.H. Xie, W. Ai, W. Huang, Kinetically controlled, scalable synthesis of gamma-FeOOH nanosheet arrays on nickel foam toward efficient oxygen evolution: the keyrole of in-situ-generated gamma-NiOOH, *Adv. Mater.* 33 (2021), 2005587, <https://doi.org/10.1002/adma.202005587>.
- [59] X.-Z. Fan, Q.-Q. Pang, S.-S. Yi, X. Du, S. Zhang, Z.-Y. Liu, X.-Z. Yue, Intrinsic-structural-modulated carbon cloth as efficient electrocatalyst for water oxidation, *Appl. Catal. B Environ.* 292 (2021), 120152, <https://doi.org/10.1016/j.apcatb.2021.120152>.
- [60] Q. Feng, Q. Wang, Z. Zhang, Y. Xiong, H. Li, Y. Yao, X.-Z. Yuan, M.C. Williams, M. Gu, H. Chen, H. Li, H. Wang, Highly active and stable ruthenate pyrochlore for enhanced oxygen evolution reaction in acidic medium electrolysis, *Appl. Catal. B Environ.* 244 (2019) 494–501, <https://doi.org/10.1016/j.apcatb.2018.11.071>.
- [61] S. Li, B. Chen, Y. Wang, M.Y. Ye, P.A. van Aken, C. Cheng, A. Thomas, Oxygen-evolving catalytic atoms on metal carbides, *Nat. Mater.* 20 (2021) 1240–1247, <https://doi.org/10.1038/s41563-021-01006-2>.